



Vlasov simulations of kinetic Alfvén waves at proton kinetic scales

C. L. Vásconez, F. Valentini, E. Camporeale, and P. Veltri

Citation: *Physics of Plasmas* (1994-present) **21**, 112107 (2014); doi: 10.1063/1.4901583

View online: <http://dx.doi.org/10.1063/1.4901583>

View Table of Contents: <http://scitation.aip.org/content/aip/journal/pop/21/11?ver=pdfcov>

Published by the AIP Publishing

Articles you may be interested in

A primitive kinetic-fluid model for quasi-parallel propagating magnetohydrodynamic waves
Phys. Plasmas **20**, 072115 (2013); 10.1063/1.4816809

Dust kinetic Alfvén and acoustic waves in a Lorentzian plasma
Phys. Plasmas **16**, 103704 (2009); 10.1063/1.3244625

Kinetic Alfvén waves and electron physics. I. Generation from ion-ion streaming
Phys. Plasmas **14**, 062104 (2007); 10.1063/1.2734950

Numerical simulation of kinetic Alfvén waves to study filament formation and their nonlinear dynamics in solar wind and corona
Phys. Plasmas **13**, 012902 (2006); 10.1063/1.2161570

Kinetic simulation of steady states of ion temperature gradient driven turbulence with weak collisionality
Phys. Plasmas **11**, 1476 (2004); 10.1063/1.1669393



SUBSCRIBE TO
physics today

Vlasov simulations of kinetic Alfvén waves at proton kinetic scales

C. L. Vásconez,^{1,2} F. Valentini,¹ E. Camporeale,³ and P. Veltri¹

¹Dipartimento di Fisica, Università della Calabria, I-87036 Cosenza, Italy

²Observatorio Astronómico de Quito, Escuela Politécnica Nacional, Quito, Ecuador

³Centrum Wiskunde & Informatica, Amsterdam, Netherlands

(Received 1 September 2014; accepted 1 November 2014; published online 12 November 2014)

Kinetic Alfvén waves represent an important subject in space plasma physics, since they are thought to play a crucial role in the development of the turbulent energy cascade in the solar wind plasma at short wavelengths (of the order of the proton gyro radius ρ_p and/or inertial length d_p and beyond). A full understanding of the physical mechanisms which govern the kinetic plasma dynamics at these scales can provide important clues on the problem of the turbulent dissipation and heating in collisionless systems. In this paper, hybrid Vlasov-Maxwell simulations are employed to analyze in detail the features of the kinetic Alfvén waves at proton kinetic scales, in typical conditions of the solar wind environment (proton plasma beta $\beta_p = 1$). In particular, linear and nonlinear regimes of propagation of these fluctuations have been investigated in a single-wave situation, focusing on the physical processes of collisionless Landau damping and wave-particle resonant interaction. Interestingly, since for wavelengths close to d_p and $\beta_p \simeq 1$ (for which $\rho_p \simeq d_p$) the kinetic Alfvén waves have small phase speed compared to the proton thermal velocity, wave-particle interaction processes produce significant deformations in the core of the particle velocity distribution, appearing as phase space vortices and resulting in flat-top velocity profiles. Moreover, as the Eulerian hybrid Vlasov-Maxwell algorithm allows for a clean almost noise-free description of the velocity space, three-dimensional plots of the proton velocity distribution help to emphasize how the plasma departs from the Maxwellian configuration of thermodynamic equilibrium due to nonlinear kinetic effects.

© 2014 AIP Publishing LLC. [<http://dx.doi.org/10.1063/1.4901583>]

I. INTRODUCTION

The solar wind is a turbulent plasma,¹ mainly composed by protons and electrons, which can be considered collisionless in good approximation. Because of the turbulent character of the interplanetary medium, the energy injected into it at large scales as Alfvénic fluctuations is transferred towards short scales along the turbulent spectrum. In such a collisionless medium, what physical mechanism drives the short-scale dissipation of the energy injected at large scales still remains an unanswered question and attracts nowadays a significant scientific interest. In fact, the identification of the fluctuations responsible for channeling the energy toward short wavelengths and the full understanding of the dissipation mechanisms in the solar wind represent two top priority subjects in space plasma physics.

The power spectrum of the solar-wind fluctuating fields in the range of long wavelengths manifests a behavior reminiscent of the $k^{-5/3}$ Kolmogorov power law for fluids,^{2–6} k being the wavenumber. The Kolmogorov-like spectral behavior extends down to a range of wavelengths close to typical proton kinetic scales (the proton inertial length d_p , and/or the proton Larmor radius ρ_p). Here, the features of the spectra abruptly change with the appearance of a spectral break^{7–9} and kinetic effects presumably govern the system dynamics.

In these range of scales and even down to typical electron kinetic scales, many solar-wind observational analyses,^{9–14} theoretical works^{15–17} and numerical simulations^{18–20} suggest that the so-called Kinetic Alfvén waves (KAWS) can play an

important role in the mechanism of turbulent energy dissipation and heating. An extensive linear analysis of these waves has been performed by Hollweg in 1999 (Ref. 21) (see also references therein for a more complete view on the subject). The fact that these fluctuations can be important in the development of the solar-wind turbulent cascade is supported by observational data which show that the distribution of wave-vectors of long wavelength magnetic fluctuations has a significant population quasi-perpendicular to the ambient magnetic field.^{22,23}

In this paper, we make use of the hybrid Vlasov-Maxwell (HVM) code,²⁴ to study numerically the characteristics of the KAWs in linear and nonlinear regime, in the range of spatial scales close to ρ_p and for $\beta_p = 1$ (for which $\rho_p \simeq d_p$). The HVM algorithm integrates numerically the Vlasov equation for the proton distribution function in multi-dimensional phase space. In the present work, we restrict our analysis to the 1D-3V (one dimension in physical space and three dimensions in velocity space) phase space configuration. Within the HVM model the electrons are considered as a fluid and a generalized Ohm equation is employed for computing the electric field, which retains the Hall term and the electron inertia effects. Quasi neutrality is assumed and the displacement current is neglected in the Ampere equation, making the assumption of low frequency dynamics. Finally, an isothermal equation of state for the scalar electron pressure is employed to close the HVM system (for more details on the HVM equations and on the numerical algorithm see Refs. 24 and 25). The HVM code is a well-tested algorithm which has been successfully

employed for numerical studies of plasma turbulence^{26–32} and ion-cyclotron heating.³³

We present the results of a series of linear and nonlinear simulations, in a situation of single-wave propagation, with a single wavenumber slightly larger than the proton skin depth wavenumber. Our goal is to perform a detailed analysis of the process of wave-particle interaction, in linear and nonlinear regime, involving resonant protons and KAWs, in typical conditions of the solar wind environment and in a range of spatial scales close to d_p . As discussed in detail in the following, our numerical results show that the efficient resonant interaction between the KAWs and the protons can significantly shape the particle distribution function, making the plasma depart from the Maxwellian configuration of thermodynamical equilibrium.

This paper is organized as follows. In Sec. II, the dispersion relation of the KAW and corresponding eigenmodes for magnetic and velocity perturbations are derived in the framework of linear two-fluid theory, under the assumptions of quasi-neutrality and negligible displacement current. Section III is devoted to the description of the hybrid Vlasov-Maxwell simulations and of the numerical results for the propagation of the KAWs, both in linear and nonlinear regimes. We conclude and summarize in Sec. IV.

II. TWO-FLUID DISPERSION RELATION AND EIGENMODES

In this section, we revisit the two-fluid approach to derive the dispersion relation and the eigenmodes of the KAWs in linear approximation. To make contact with the HVM model, the set of linear two-fluid (protons and electrons) equations have been solved under the assumption of quasi-neutrality ($n_e \simeq n_p = n$) and by neglecting the displacement current in the Ampere equation. Moreover, proton and electron scalar pressures have been assigned a general adiabatic equation of state. This analysis allows us to specialize to the hybrid case the linear expectations for the wave frequency of KAWs obtained in previous works (see, for instance, Ref. 21). The linear results obtained in this section will be used to guide the HVM simulations discussed in detail in the following. In particular, the linear frequency and the expressions of the eigenmodes for the KAW branch will be employed to initialize the HVM simulations both in linear and nonlinear regime.

We choose the reference frame pictured in Fig. 1, in which the wave vector $\mathbf{k} = (k, 0, 0)$ is along the positive x direction and the background magnetic field $\mathbf{B}_0 = (B_{0x}, B_{0y}, 0)$ lies in the x - y plane, inclined at an angle θ with respect to the x axis. In these conditions the problem is intrinsically one dimensional in physical space.

By coupling the continuity equations for particle density and momentum equations to Maxwell equations for fields, under the assumptions discussed above, after some algebra, one can obtain the dimensionless wave dispersion relation in the form of a sixth-order polynomial equation, which can be written as

$$A\omega^6 + B\omega^4 + C\omega^2 + D = 0, \quad (1)$$

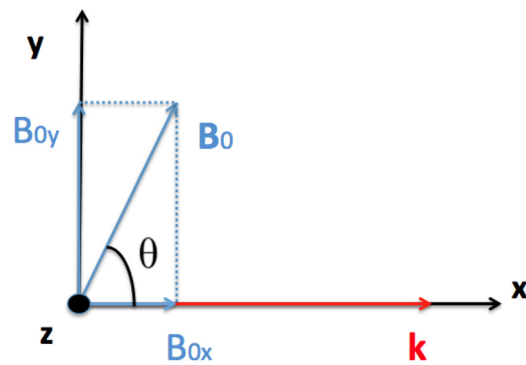


FIG. 1. The reference frame chosen for the study of KAWs; the wavevector \mathbf{k} is along the x direction, while the background magnetic field \mathbf{B}_0 lies in the x - y plane, inclined at an angle θ with respect to \mathbf{k} .

where

$$\begin{aligned} A &= (1 + k^2 d_e^2)^2, \\ B &= -(1 + k^2 d_e^2)k^2[1 + \cos^2 \theta + \beta(1 + k^2 d_e^2)] \\ &\quad - k^4 \cos^2 \theta, \\ C &= k^4 \cos^2 \theta[1 + \beta k^2 + 2\beta(1 + k^2 d_e^2)], \\ D &= \beta k^6 \cos^4 \theta, \end{aligned}$$

where β is the total plasma beta.

The above equations have been rescaled by normalizing time by the inverse proton cyclotron frequency Ω_{cp}^{-1} , velocities by the Alfvén speed V_A , mass by the proton mass m_p , and lengths by the proton inertial length $d_p = V_A/\Omega_{cp}$. In these units, the electron inertial length is given by $d_e = (m_e/m_p)^{1/2}$. Also, the modulus of the background magnetic field is set $B_0 = 1$. For now on, all physical quantities will be rescaled by the characteristic parameters listed previously.

Equation (1) can be solved analytically by making use of the so-called Vieta's substitution,³⁴ to obtain values of the wave frequencies for any given angle θ , any value of β and for any range of wave numbers. In Fig. 2, we show, in a logarithmic plot, the three roots of Eq. (1), obtained for positive

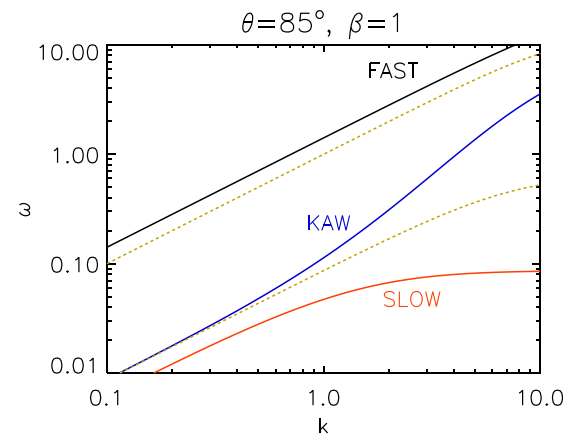


FIG. 2. The three roots of Eq. (1), i.e., FAST (black-solid curve), SLOW (red-solid curve), and KAW (blue-solid curve) branches, for $\theta = 85^\circ$, $\beta = 1$ and in the range of wavenumbers around $k = 1$. The yellow-dashed curves represent the solutions of Eq. (1), in the case of cold plasma ($\beta \ll 1$), for which the SLOW branch disappears.

values of ω , for a specific case with $\theta = 85^\circ$ and $\beta = 1$, in the range of wavenumbers around the proton skin depth wavenumber ($k = 1$). In this plot, the black (red) solid line represents the branch of fast (slow) magnetosonic waves, while the blue solid line refers to the KAW branch. The yellow-dashed curves are the solutions obtained under the cold plasma approximation ($\beta \ll 1$), for which the slow magnetosonic branch disappears.

Moreover, from the analysis of the linearized two-fluid equations, one can also get explicit expressions of the eigenmodes for magnetic ($\delta\mathbf{B}$) and velocity ($\delta\mathbf{u}$) perturbations, which read

$$\delta B_z = 2a \cos(kx), \quad (2)$$

$$\delta B_y = -\frac{\cos \theta}{\omega} \left[1 - \frac{\omega^2(1+k^2d_e^2)}{k^2 \cos^2 \theta} \right] 2a \sin(kx), \quad (3)$$

$$\delta u_z = -\frac{k \cos \theta}{\omega} 2a \cos(kx), \quad (4)$$

$$\delta u_y = \frac{k \cos^2 \theta}{\omega^2} \left[1 - \frac{\omega^2(1+k^2d_e^2)}{k^2 \cos^2 \theta} \right] 2a \sin(kx), \quad (5)$$

$$\delta u_x = \frac{k \sin(2\theta)}{2(\omega^2 - \beta k^2)} \left[1 - \frac{\omega^2(1+k^2d_e^2)}{k^2 \cos^2 \theta} \right] \times 2a \sin(kx), \quad (6)$$

where a is a real number.

It is worth noting from the expressions above that the magnetic and the velocity eigenmodes have elliptic polarization and a $\pi/2$ phase displacement.

The previous expressions for magnetic and velocity perturbations will be used to initialize the HVM simulations of KAWs, presented in Sec. III. Clearly, Eqs. (2)–(6) are not exact eigenmodes of the HVM equations; nevertheless, as we will show in the following, when used as initial perturbations in the HVM simulations, they allow to excite predominantly one desired wave mode, by selecting the appropriate value of ω for a given k . For our purpose of studying numerically the features of the KAWs, this is crucial since it prevents the excitation of mixture of modes which would complicate the analysis.

III. HYBRID VLASOV-MAXWELL SIMULATIONS

We solve numerically the HVM equations²⁴ in 1D-3 V phase space configuration. The set of HVM equations in dimensionless units can be summarized in the form

$$\frac{\partial f}{\partial t} + \mathbf{v} \cdot \nabla f + (\mathbf{E} + \mathbf{v} \times \mathbf{B}) \cdot \frac{\partial f}{\partial \mathbf{v}} = 0, \quad (7)$$

$$\mathbf{E} - d_e^2 \Delta \mathbf{E} = -(\mathbf{u} \times \mathbf{B}) + \frac{1}{n} (\mathbf{j} \times \mathbf{B}) - \frac{1}{n} \nabla P_e + \frac{d_e^2}{n} \left[\nabla \cdot \Pi + \nabla \cdot (\mathbf{u}\mathbf{j} + \mathbf{j}\mathbf{u}) - \nabla \cdot \left(\frac{\mathbf{j}\mathbf{j}}{n} \right) \right], \quad (8)$$

$$\frac{\partial \mathbf{B}}{\partial t} = -\nabla \times \mathbf{E}; \quad \nabla \times \mathbf{B} = \mathbf{j}, \quad (9)$$

where f is the proton distribution function, \mathbf{E} and \mathbf{B} the electric and magnetic fields, respectively, and \mathbf{j} the total current

density (the displacement current has been neglected in the Ampere equation and quasi-neutrality is assumed). In Eq. (8) the following compact notations have been used (see Ref. 24 for more details):

$$[\nabla \cdot (\mathbf{u}\mathbf{j} + \mathbf{j}\mathbf{u})]_i = \frac{\partial}{\partial x_i} (u_i j_j + j_i u_j), \quad (10)$$

$$\left[\nabla \cdot \left(\frac{\mathbf{j}\mathbf{j}}{n} \right) \right]_i = \frac{\partial}{\partial x_i} \left(\frac{j_i j_j}{n} \right). \quad (11)$$

In 1D-3 V configuration, the spatial variations occur along the x -direction, but each vector has three components; in this case, $\nabla = d/dx$, $\Delta = d^2/dx^2$. The proton density n , bulk velocity \mathbf{u} , and pressure tensor Π are obtained as velocity moments of f . The scalar electron pressure P_e is assigned an isothermal equation of state $P_e = nT_e$, where T_e is the electron temperature. As in Sec. II, the background magnetic field is chosen to lie in the x - y plane (see Fig. 1).

The numerical algorithm employed to solve the above HVM Eqs. (7)–(9) is based on the coupling of the well-known splitting method³⁵ and the Current Advance Method³⁶ for the electromagnetic fields, generalized to the hybrid case in Ref. 24. Periodic boundary conditions are employed in physical space, while in the velocity domain the distribution function is set equal to zero at $|v| > v_{max}$, where v_{max} fixes the limits of the numerical domain in each velocity direction. For each simulation discussed in the following, the time step Δt has been chosen in such a way to satisfy the Courant-Friedrichs-Levy condition,³⁷ for the numerical stability of time explicit finite difference algorithms.

A. Linear regime

The numerical analysis of the linear regime of wave propagation, presented in this section, is preparatory for the study of the nonlinear regime discussed in the following. These preliminary simulations can be, therefore, considered as a benchmark to show that the HVM code is able to describe properly the evolution of the KAWs and that the numerical resolution employed is adequate to ensure a satisfactory conservation of the HVM invariants (energy, mass, entropy).

For the analysis of the linear regime, we simulate a plasma embedded in a uniform magnetic field $\mathbf{B}_0 = B_{0x}\mathbf{e}_x + B_{0y}\mathbf{e}_y$ (see Fig. 1). At $t = 0$, protons have homogeneous and constant density and Maxwellian distribution of velocities. We set $\beta_p = 2v_{thp}^2/V_A^2 = 1$ (v_{thp} being the proton thermal speed), while the electron to proton temperature ratio is $T_e/T_p = 1$ and the proton to electron mass ratio is set $m_p/m_e = 100$ (we point out that, for a realistic mass ratio, the electron skin depth d_e cannot be adequately resolved with the numerical resolution chosen for the HVM simulations). This initial condition is perturbed at $t = 0$ by imposing on the system the magnetic and velocity perturbations in Eqs. (2)–(6), calculated for the KAW solution, with $a = 10^{-5}$ and $k = mk_0$, where $k_0 = 2\pi/L$ is the fundamental wave number; we fixed $m = 6$, thus $k = 3d_p^{-1}$.

The length of the spatial box is $L = 4\pi$, while $v_{max} = 4.5v_{thp}$ in each velocity direction. The numerical 1D-3 V

phase space domain is discretized by $N_x = 512$ grid points in physical space and $N_{V_y} = N_{V_z} = 41$ grid points along the v_y and v_z directions. The number of grid points used to discretized the v_x direction has been chosen in such a way to avoid effects of numerical recurrence. In fact, in the case of very weak electric and magnetic fields, as it happens in linear regime, Eq. (7) describes a motion close to free streaming and its solution, in 1D physical space, can be written as $f_k(v, t) = f_0(v) \exp[ik(x - vt)]$. If the mesh spacing in the v_x velocity direction is $\Delta v_x = 2v_{max}/N_{V_x}$, there is a numerical recurrence occurring at $T_R = 2\pi/(k\Delta v_x)$. Therefore, if t_{max} is the maximum time of the simulation, Δv_x must be chosen in such a way that $t_{max} < T_R$, for a fixed value of k . For example, for $t_{max} = 125$, $k = 3$ and $v_{max} = 4.5v_{thp}$, one must choose $N_{V_x} = 401$ in such a way to have $T_R \simeq 132 > t_{max}$.

From linear kinetic plasma theory,³⁸ small-amplitude waves in a uniformly magnetized plasma undergo Landau damping if they have a component of propagation along the background magnetic field \mathbf{B}_0 ; only particle moving along \mathbf{B}_0 contribute to damping, because in a uniform magnetic field there is no net motion of particles across the field. In order to analyze the effects of Landau damping³⁹ on the KAW oscillations, as dependent on the propagation angle with respect to \mathbf{B}_0 , we performed 14 simulations for different values of θ (the angle between the wave vector and the background magnetic field) in the range $69^\circ \leq \theta \leq 85^\circ$. In Fig. 3 we report, in semilogarithmic plot, the time evolution of the absolute value of the $m = 6$ Fourier component of the magnetic fluctuation $\delta B_{z,k}(m = 6, t)$, normalized to its value at $t = 0$, for $\theta = 81^\circ, 83^\circ, 85^\circ$ (blue-solid, red-solid, and black-solid line, respectively). In agreement with linear kinetic theory,³⁸ the oscillation amplitude decays exponentially in time, the damping rate γ appearing strongly dependent on θ (the smaller θ , the larger γ). Note that for the simulation with $\theta = 85^\circ$ we fixed $t_{max} = 125$, while simulations with smaller θ , for which heavily damped oscillations are recovered, have been stopped at earlier time. The blue-dashed, red-dashed, and black-dashed lines in this figure represent the best fits for the damping rates of the oscillations, whose absolute

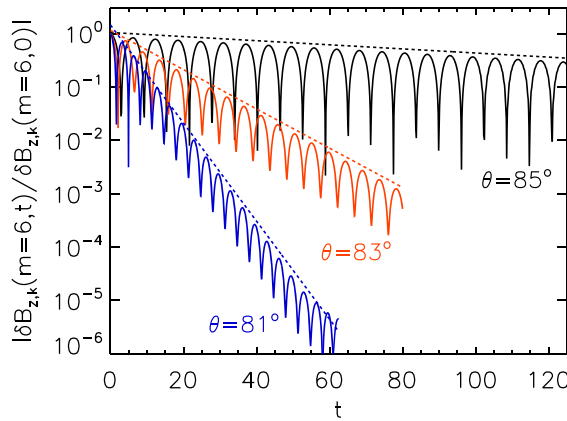


FIG. 3. Time evolution of $|\delta B_{z,k}(m = 6, t)/\delta B_{z,k}(m = 6, 0)|$, for $a = 10^{-5}$ and for $\theta = 81^\circ, 83^\circ, 85^\circ$ (blue-solid, red-solid, and black-solid line, respectively). The blue-dashed, red-dashed, and black-dashed lines represent the best fits for the damping rates of the oscillations.

values result $|\gamma| \simeq 0.24, 0.085, 0.009$ for $\theta = 81^\circ, 83^\circ, 85^\circ$, respectively.

In order to show that the oscillations recovered in our simulations are in fact KAWs, we have, first of all, performed a Fourier analysis of the numerical signals, from which we found that (i) no time transient is observed in the wave oscillations and (ii) the $\omega-k$ spectrum displays a single excited wavenumber, to which corresponds a single dominant frequency peak (secondary peaks have energy content more than 10^4 times lower than the dominant one). This means that even starting with a two-fluid initial condition, a well defined kinetic normal mode has been excited. Moreover, in Fig. 4, we plot the numerical results for the oscillation frequency ω [blue diamonds in panel (a)], and for the absolute value of the damping rate $|\gamma|$ [blue diamonds in panel (b)], as functions of θ , for the 14 simulations performed. In panel (a), we also reported the theoretical prediction for $\omega = \omega(\theta)$ on the KAW branch obtained from the two-fluid approach (black-solid curve) discussed in Sec. II [see Eq. (1)] and from a kinetic linear Vlasov solver (red-solid curve). In panel (b), the solution of $|\gamma| = |\gamma(\theta)|$ for the KAW branch, obtained from a kinetic linear Vlasov solver,

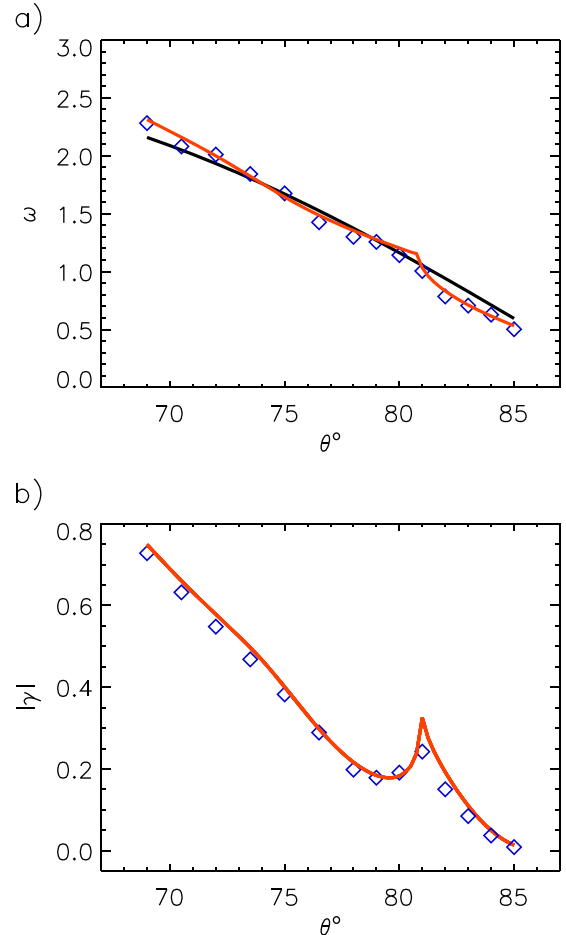


FIG. 4. Panel (a): dependence of the wave frequency ω on the propagation angle θ , obtained from the linear HVM simulations (blue diamonds), linear two-fluid theory (black-solid curve) and linear kinetic Vlasov solver (red-solid curve). Panel (b): dependence of the absolute value of the damping rate $|\gamma|$ on θ , obtained from the linear HVM simulations (blue diamonds) and from the linear kinetic Vlasov solver (red-solid curve).

is indicated by a red-solid curve. We note that the linear Vlasov solutions have been obtained by employing the standard kinetic theory for an electron-proton plasma.⁴⁰ However, in order to mimic the HMV system, we have considered the limit $m_e/m_p \rightarrow 0$. Panels (a) and (b) in Fig. 4 show a nice agreement between numerical results and analytical (two-fluid and kinetic) predictions, demonstrating that the fluctuations recovered in our HVM simulations can be identified as KAWs.

To conclude this section, we shortly discuss the conservation of the HVM invariants during the simulations. In particular, we consider the conservation of proton mass and entropy and total energy. Concerning the latter quantity, we point out that for the HVM Eqs. (7)–(9), a standard conservation law cannot be derived for the total energy, as a consequence of neglecting the displacement current in the Ampere equation. In fact, by multiplying the proton Vlasov Eq. (7) by $v^2/2$, through integration over the whole velocity space and over the 1D periodic spatial domain $D = [0, L]$ (the result can be easily generalized to the 3D case in physical space), one gets the following dimensionless equation:

$$\int_0^L \left[\frac{\partial}{\partial t} \left(\frac{3}{2} n T_p + \frac{1}{2} n u^2 + \frac{B^2}{2} \right) + \mathbf{E} \cdot \mathbf{j}_e \right] dx = 0, \quad (12)$$

where $\mathbf{j}_p = n \mathbf{u}$ and $\mathbf{j}_e = \nabla \times \mathbf{B} - \mathbf{j}_p$ are proton and electron current densities, respectively (we remind the reader that in scaled units the proton mass is $m_p = 1$ and the proton electric charge is $e = 1$). In Eq. (12) one recognizes the contribution of the thermal energy density $3/2nT_p$, of the kinetic energy density $1/2nu^2$ and of the magnetic energy density $B^2/2$, while the term $\mathbf{E} \cdot \mathbf{j}_e$ represents the work of the electric field on the electrons.

As anticipated before, Eq. (12) is not in the usual form of conservation law; nevertheless, if one sets

$$L_e = \int_0^L dx \int_0^t \mathbf{E} \cdot \mathbf{j}_e dt'; \quad E_M = \int_0^L \frac{B^2}{2} dx, \quad (13)$$

$$E_{kin} = \int_0^L \frac{n u^2}{2} dx; \quad E_{th} = \int_0^L \frac{3 n T_p}{2} dx. \quad (14)$$

Eq. (12) can be re-written in the following form:

$$\frac{\partial}{\partial t} (L_e + E_{th} + E_{kin} + E_M) = 0 \quad (15)$$

or, equivalently, as

$$E_{tot} = L_e + E_{th} + E_{kin} + E_M = \text{const}. \quad (16)$$

The quantities L_e , E_M , E_{th} , and E_{kin} can be evaluated at each time step in the HVM simulations, in such a way to control the conservation of E_{tot} .

For the linear simulations discussed in this section, typical relative mass variations are limited to $\sim 10^{-5}\%$, entropy variations to $\sim 0.036\%$ and total energy variations to $\sim 0.088\%$, confirming the adequacy of the numerical resolution adopted and the reliability of the numerical results.

B. Nonlinear regime

To investigate the nonlinear regime of propagation of the KAWs, we considered six different simulations, whose typical parameters (β_p , T_e/T_p , m_p/m_e), initial condition and initial magnetic and velocity perturbations are the same as those described in Sec. III A, except for the amplitude of the perturbations that is set now $a = 0.15, 0.17, 0.19, 0.21, 0.23, 0.25$, respectively. The length of the spatial box is, as for the linear simulations, $L = 4\pi$, while we set $v_{max} = 5v_{thp}$. The number of grid points in the spatial domain is $N_x = 512$ and in the three-dimensional velocity domain we set $N_{V_x} = N_{V_y} = N_{V_z} = 91$. These nonlinear simulations follow the plasma dynamics up to a time $t_{max} = 1000$. The typical relative variations of mass, energy, and entropy for these nonlinear simulations are $\sim 10^{-3}\%$, $\sim 1\%$, and 0.8% , respectively. We point out that in nonlinear regime possible numerical recurrence phenomena cannot be controlled in a simple way, since, for large amplitudes of the electric and magnetic fields, the particle motion can no longer be approximated as free-streaming. However, the satisfactory conservation of the Vlasov invariants attests the reliability of the numerical results.

In order to compare the evolution of the magnetic fluctuations for large initial perturbation amplitudes with that obtained in linear regime, in Fig. 5 we plot $\delta B_{z,k}(m=6,t)$, for $\theta = 85^\circ$, in the cases with $a = 0.15$ [panel (a)] and $a = 0.25$ [panel (b)]. In the linear case (see Fig. 3), the magnetic oscillations for $\theta = 85^\circ$ appear exponentially damped up to a time $t = 120$. On the other hand, in the nonlinear regime pictured

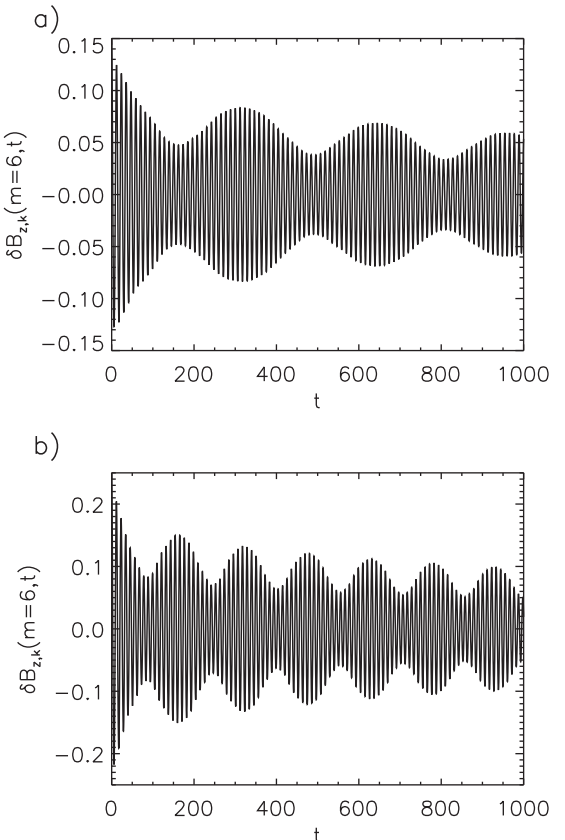


FIG. 5. Time evolution of $\delta B_{z,k}(m=6,t)$, for $a = 0.15$ [panel (a)] and $a = 0.25$ [panel (b)], and for $\theta = 85^\circ$.

in Fig. 5, after a preliminary stage of exponential decay of the wave amplitude, Landau damping is saturated by nonlinear effects and, for both $a=0.15$ and $a=0.25$, the magnetic fluctuations display characteristic envelope oscillations, whose period appears to be inversely proportional to a (larger values of a correspond to smaller envelope oscillation periods). It is worth noting that no decay instability toward smaller wavenumbers has been recovered during the simulation, even though the wavelength of the imposed perturbations is not the largest wavelength that fits in the spatial simulation box; the KAW mode excited at $t=0$ remains dominant with a small amount of energy stored in its harmonics.

The phenomenology described above is clearly reminiscent of the nonlinear saturation of Landau damping of electrostatic waves, due to particle trapping.^{41–44} We analyzed in detail the dependence of the period τ of the envelope oscillations displayed in Fig. 5 on the amplitude a of the initial perturbations. Assuming a relation of the type $\tau=a^p$, in Fig. 6 we show $\ln(\tau)$ versus $\ln(a)$ for the six nonlinear simulations (black stars). The red-dashed line in this figure represents the best fit of the numerical data; the best-fitting procedure gives a value $p=-1.23$.

Simple arguments help to understand how protons can be trapped by a pseudo-potential and give rise to envelope oscillations in the wave amplitude, as shown in Fig. 5 and in analogy with the electrostatic case. Assuming spatial variations only in the x direction, in a reference frame moving with the wave phase speed v_ϕ , the electric potential ϕ can be seen as a static potential, depending only on a single variable $\xi=x-v_\phi t$. For a single proton with velocity $\mathbf{v}=(v_x, v_y, v_z)$, one can then derive a dimensionless energy conservation law, in the form

$$\mathcal{E} = \frac{(v_x - v_\phi)^2 + v_y^2 + v_z^2}{2} + \phi(\xi) = \text{const}, \quad (17)$$

$$\phi(\xi) = - \int_{\xi_0}^{\xi} E_x(\xi') d\xi', \quad (18)$$

ξ_0 being an arbitrary constant.

Moreover, conservation equations for the canonical momentum in y and z directions can be used

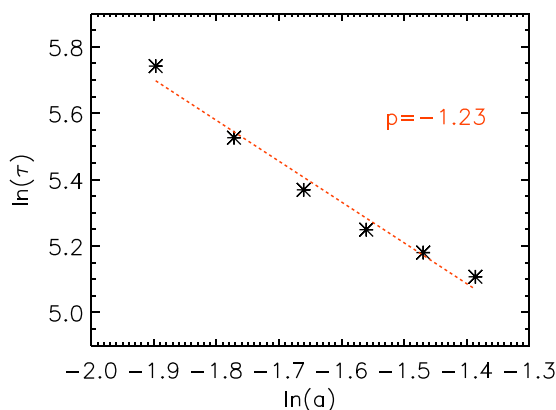


FIG. 6. Dependence of the logarithm of the wave envelope oscillation period on the logarithm of the initial perturbation amplitude.

$$v_y + A_y(\xi) = v_{y0}; \quad v_z + A_z(\xi) = v_{z0}, \quad (19)$$

$$A_y(\xi) = \int_{\xi_0}^{\xi} B_z(\xi') d\xi', \quad (20)$$

$$A_z(\xi) = - \int_{\xi_0}^{\xi} B_y(\xi') d\xi', \quad (21)$$

v_{y0} and v_{z0} being two constants, and $A_y(\xi)$, $A_z(\xi)$ the y and z components of the magnetic potential. Eqs. (19) allow to express $(v_y^2 + v_z^2)/2$ as a function of ξ and, from Eq. (17), one gets

$$\begin{aligned} \mathcal{E}(\xi, v_x) &= \frac{(v_x - v_\phi)^2}{2} + \phi(\xi) + \frac{1}{2} [v_{y0} - A_y(\xi)]^2 \\ &\quad + \frac{1}{2} [v_{z0} - A_z(\xi)]^2 = \text{const}. \end{aligned} \quad (22)$$

The above equation can be re-written as

$$\mathcal{E}(\xi, v_x) = \frac{(v_x - v_\phi)^2}{2} + \Phi(\xi) = \text{const}. \quad (23)$$

Here, $\Phi(\xi) = \phi(\xi) + [v_{y0} - A_y(\xi)]^2/2 + [v_{z0} - A_z(\xi)]^2/2$ can be viewed as a pseudo-potential which can trap resonant protons.

As the HVM code allows for a clean low-noise description of the proton distribution function, the role of nonlinear kinetic effects on the plasma dynamics, and in particular of the trapping of protons in the pseudo-potential Φ , can be directly observed in phase space contour plots or in three-dimensional velocity iso-surface plots of f .

In Fig. 7, we report the $x - v_x$ level lines of f calculated at $v_y = v_z = 0$ (i. e., we selected the phase space along the direction of \mathbf{k}) at four different times for the simulation with $a=0.25$ ($t=300, 500, 700, 1000$ from top to bottom). The phase velocity of the fluctuations, evaluated through the Fourier analysis on the numerical signals, is $\omega/k \simeq 0.2$. In panel (a) of Fig. 7, vortical phase space structures are clearly visible in the velocity range around $v_x=0$. These phase space vortices are typical signature of the presence of trapped particle populations.^{42–44} The resulting complicated phase space contour lines of f are determined by the nonlinear interaction and beating of two counter-propagating signals (in our initial condition both positive and negative values of the wavenumber are excited for a given positive frequency). At larger times, in panel (b), (c), and (d), the phase space structures with positive mean velocity move along the positive x direction, while the ones with negative mean velocity move in the negative x direction, giving rise to different phase space shapes. Due to the fact that the phase velocity of the fluctuations is small compared to both V_A and v_{thp} , these strong phase space distortions are located in the middle of the core of the proton distribution function, confined in the velocity range $-1 \leq v_x \leq 1$ for each spatial position.

Figure 8 shows four different slices of the $x - v_x$ proton distribution function at $t=300$, evaluated at four different spatial positions $x_0 \simeq 2.5, 3.5, 8.5, 10$ (red, black, blue, and

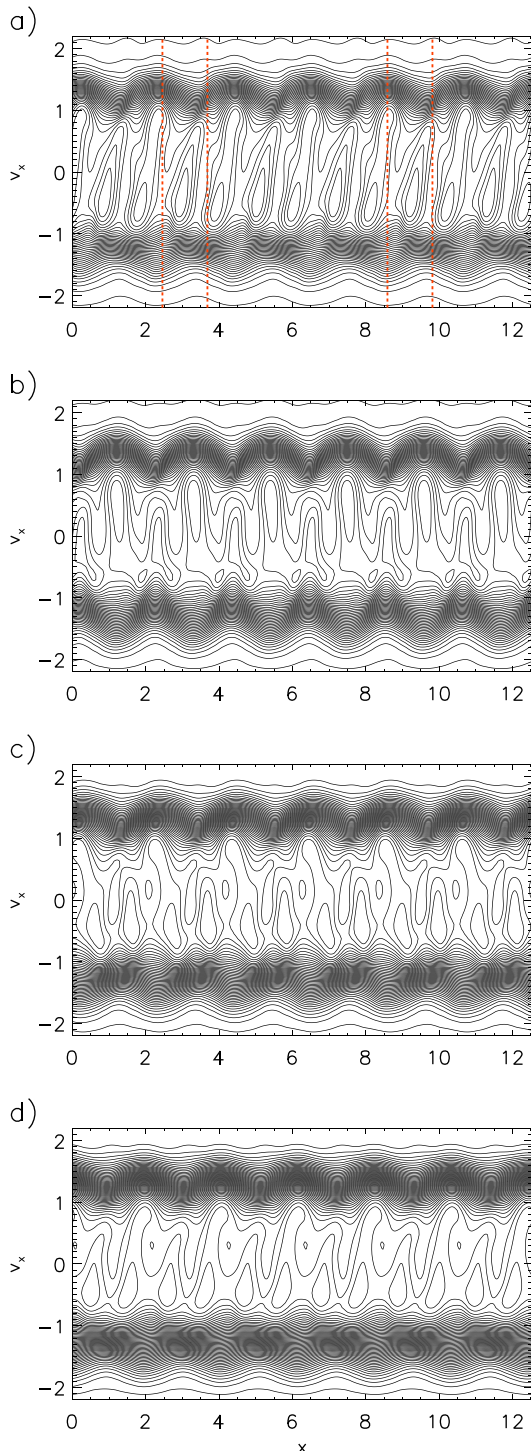


FIG. 7. $x - v_x$ level lines of the proton distribution function f calculated at $v_y = v_z = 0$ at four different times $t = 300, 500, 700, 1000$ (from top to bottom), for the nonlinear simulation with $a = 0.25$.

green, respectively), indicated by vertical red-dashed lines in Fig. 7(a). It is clear from the curves in Fig. 8 that the nonlinear wave-particle interaction, occurred in the velocity range $-1 \leq v_x \leq 1$, has produced peculiar flat-top velocity profiles, by flattening the peak of the v_x proton velocity distribution. It is worth to point out that the velocity width of the flat-top region is nearly independent on x , as it can be deduced from Fig. 8.

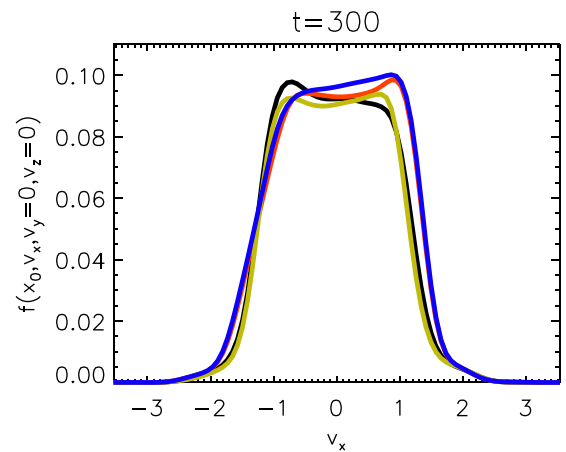


FIG. 8. v_x profiles of the proton distribution function f calculated at $v_y = v_z = 0$ and at four different spatial positions $x_0 \approx 2.5, 3.5, 8.5, 10$ (red, black, blue, and green, respectively) for the nonlinear simulation with $a = 0.25$, at $t = 300$.

Finally, in Fig. 9, we report the velocity iso-surfaces of the proton distribution function at $t = 300$ evaluated at the spatial locations $x_0 \approx 2.5, 3.5, 8.5, 10$ (top-left, top-right, bottom-left, bottom-right, respectively). In these three-dimensional plots it is clearly visible that the flattening along the v_x direction, produced by nonlinear effects as discussed above, makes the 3D proton velocity distributions look like flat disks (or pancakes), almost independently on the spatial location x_0 at which the 3D plot is considered. It is also worth noting that the ring-like modulations of the 3D velocity distributions along the v_y axis (especially visible in the top-right and bottom-right panels) presumably indicate v_y resonance velocity shells. We note that in two recent papers by Rudakov *et al.*,^{45,46} the linear and nonlinear Landau resonance of KAW fluctuations and the consequent evolution of the particle distribution functions have been analyzed; in these works, it is shown how KAW turbulence in the solar wind can lead to the generation of non-Maxwellian distribution functions, with the formation of velocity plateaus which, in turn, decrease the Landau damping rate of the fluctuations.

To conclude this section, we performed a numerical simulation of collisional relaxation for one of the non-Maxwellian velocity distributions of Fig. 9, in presence of Coulomb proton-proton collisions modeled by the full Landau integral.^{47–49} From this analysis, performed using typical parameters of the solar-wind environment, we estimated the characteristic time of relaxation towards a Maxwellian for the considered velocity distribution. This characteristic time results about 10^5 times larger than the proton gyro period; this suggests that the velocity distributions produced in our simulations by resonant interaction of protons with KAW fluctuations are stable against collisions and thus likely to be observed in *in situ* measurements from spacecraft.

IV. SUMMARY AND CONCLUSIONS

In this paper, we have analyzed numerically the kinetic features of the KAWs at large propagation angles, in typical

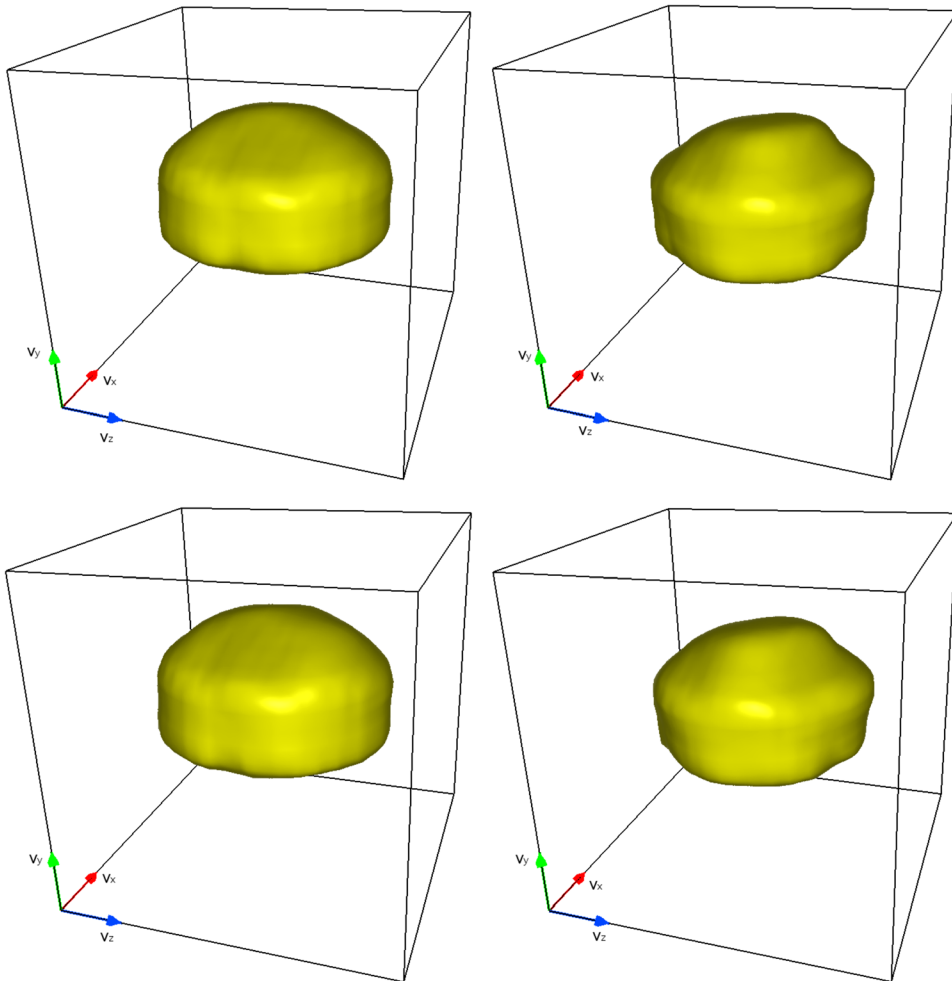


FIG. 9. Three-dimensional iso-surface plots of the proton velocity distribution at four different spatial positions $x_0 \approx 2.5, 3.5, 8.5, 10$ (top-left, top-right, bottom-left, bottom-right, respectively), for the nonlinear simulation with $a = 0.25$, at $t = 300$.

conditions of the solar-wind environment, by employing the kinetic hybrid Vlasov-Maxwell code²⁴ in 1D-3V phase space configuration. Our kinetic simulations in nonlinear regime have been guided by a preliminary analysis of the two-fluid theory for the KAWs and by a set of linear simulations which helped us to choose the simulation parameters, the initial condition, the numerical resolution and the form of the initial perturbations, in such a way to focus our study on the propagation of a monochromatic KAW.

While in linear regime the amplitude of the oscillations undergoes collisionless Landau damping, whose effect is larger for smaller propagation angles θ , in the case of large initial amplitude perturbations, the effects of damping is saturated. Then, the wave amplitude starts oscillating around an almost constant level with a period τ , inversely proportional to the initial perturbation amplitude. This phenomenology is clearly reminiscent of the nonlinear saturation of Landau damping in the electrostatic case, due to particle trapping.⁴¹ In fact, also for the case of the KAW it is possible to show that resonant protons can be trapped by a pseudo-potential and presumably trigger a physical process analogous to the trapping of particles in an electrostatic potential well.

Thanks to the fact that the Eulerian HVM algorithm provides a clean noise-free description of the phase space plasma dynamics, we pointed out how the resonant interaction between KAWs and protons can give rise to significant deformations of the proton distribution function, appearing

as phase space vortices and complicated structures. In particular, peculiar flat-top velocity profiles have been recovered in the velocity direction parallel to the wavevector. Moreover, the three-dimensional iso-surface plots in velocity space have revealed that the proton velocity distribution assumes the typical shape of a flat disk, remarkably departing from the spherical isotropic Maxwellian configuration.

Finally, the numerical simulations presented in this paper suggest that when nonlinear processes of resonant wave-particle interaction are at play, describing the entire three-dimensional velocity domain is crucial, since it allows the particle velocity distribution to freely model its shape, in response to its interaction with a large amplitude wave. The results discussed in this paper are especially relevant in the field of space plasma physics, where the KAWs have recently gained an important role in the study of solar-wind turbulence dissipation and heating,^{9–20} at typical proton and electron kinetic scales.

ACKNOWLEDGMENTS

The numerical simulations discussed in the present paper have been run on the Fermi supercomputer at CINECA (Bologna, Italy), within the ISCRA Class C Project IsC15-KAWVLAS. F.V. and E.C. acknowledge the participation to the ISSI International Team 292 “Kinetic Turbulence and Heating in the Solar Wind.”

- ¹E. Marsch, *Living Rev. Solar Phys.* **3**, 1 (2006); R. Bruno and V. Carbone, *ibid.* **2**, 4 (2005).
- ²A. N. Kolmogorov, *Dokl. Akad. Nauk SSSR* **30**, 299 (1941).
- ³P. J. Coleman, *Astrophys. J.* **153**, 371 (1968).
- ⁴M. Dobrowolny, A. Magneney, and P. Veltri, *Phys. Rev. Lett.* **45**, 144 (1980).
- ⁵C. Y. Tu and E. Marsch, *Space Sci. Rev.* **73**, 1 (1995).
- ⁶M. Goldstein, D. A. Roberts, and W. H. Matthaeus, *Annu. Rev. Astron. Astrophys.* **33**, 283 (1995).
- ⁷R. J. Leamon, W. H. Matthaeus, and C. W. Smith, *Astrophys. J.* **537**, 1054 (2000).
- ⁸S. Bourouaine, S. Alexandrova, E. Marsch, and M. Maksimovic, *Astrophys. J.* **749**, 102 (2012).
- ⁹S. D. Bale, P. J. Kellogg, F. S. Mozer, T. S. Horbury, and H. Reme, *Phys. Rev. Lett.* **94**, 215002 (2005).
- ¹⁰F. Sahraoui, M. L. Goldstein, P. Robert, and Yu. V. Khotyaintsev, *Phys. Rev. Lett.* **102**, 231102 (2009).
- ¹¹J. J. Podesta and J. M. Tenbarge, *J. Geophys. Res.* **117**, A10106, doi:10.1029/2012JA017724 (2012).
- ¹²C. S. Salem, G. G. Howes, D. Sundkvist, S. D. Bale1, C. C. Chaston, C. H. K. Chen, and F. S. Mozer, *Astrophys. J. Lett.* **745**, L9 (2012).
- ¹³C. H. K. Chen, S. Boldyrev, Q. Xia, and J. C. Perez, *Phys. Rev. Lett.* **110**, 225002 (2013).
- ¹⁴K. H. Kiyani, S. C. Chapman, F. Sahraoui, B. Hnat, O. Fauvarque, and Yu. V. Khotyaintsev, *Astrophys. J.* **763**, 10 (2013).
- ¹⁵G. G. Howes, S. C. Cowley, W. Dorland, G. W. Hammett, E. Quataert, and A. A. Schekochihin, *J. Geophys. Res.* **113**, A05103, doi:10.1029/2007JA012665 (2008).
- ¹⁶A. A. Schekochihin, S. C. Cowley, W. Dorland, G. W. Hammett, G. G. Howes, E. Quataert, and T. Tatsuno, *Astrophys. J.* **182**, 310 (2009).
- ¹⁷F. Sahraoui, G. Belmont, and M. L. Goldstein, *Astrophys. J.* **748**, 100 (2012).
- ¹⁸S. P. Gary and K. Nishimura, *J. Geophys. Res.* **109**, A02109, doi:10.1029/2003JA010239 (2004).
- ¹⁹G. G. Howes, W. Dorland, S. C. Cowley, G. W. Hammett, E. Quataert, A. A. Schekochihin, and T. Tatsuno, *Phys. Rev. Lett.* **100**, 065004 (2008).
- ²⁰J. M. TenBarge and G. G. Howes, *Phys. Plasmas* **19**, 055901 (2012).
- ²¹J. V. Hollweg, *J. Geophys. Res.* **104**(A7), 14811, doi:10.1029/1998JA900132 (1999).
- ²²W. H. Matthaeus, M. L. Goldstein, and J. H. King, *J. Geophys. Res.* **91**, 59, doi:10.1029/JA091iA01p00059 (1986).
- ²³W. H. Matthaeus, M. L. Goldstein, and D. A. Roberts, *J. Geophys. Res.* **95**, 20673, doi:10.1029/JA095iA12p20673 (1990).
- ²⁴F. Valentini, P. Travnicek, F. Califano, P. Hellinger, and A. Mangeney, *J. Comput. Phys.* **225**, 753 (2007).
- ²⁵F. Valentini, P. Veltri, and A. Mangeney, *J. Comput. Phys.* **210**, 730 (2005).
- ²⁶F. Valentini, F. Califano, and P. Veltri, *Phys. Rev. Lett.* **104**, 205002 (2010).
- ²⁷S. Servidio, F. Valentini, F. Califano, and P. Veltri, *Phys. Rev. Lett.* **108**, 045001 (2012).
- ²⁸S. Servidio, K. T. Osman, F. Valentini, D. Perrone, F. Califano, S. Chapman, W. H. Matthaeus, and P. Veltri, *Astrophys. J. Lett.* **781**, L27 (2014).
- ²⁹W. H. Matthaeus, S. Oughton, K. T. Osman, S. Servidio, M. Wan, S. P. Gary, M. A. Shay, F. Valentini, V. Roytershteyn, H. Karimabadi, and S. C. Chapman, *Astrophys. J.* **790**, 155 (2014).
- ³⁰F. Valentini, A. Vecchio, S. Donato, V. Carbone, C. Briand, J. Bougeret, and P. Veltri, *Astrophys. J. Lett.* **788**, L16 (2014).
- ³¹A. Greco, F. Valentini, S. Servidio, and W. H. Matthaeus, *Phys. Rev. E* **86**, 066405 (2012).
- ³²D. Perrone, F. Valentini, S. Servidio, S. Dalena, and P. Veltri, *Astrophys. J.* **762**, 99 (2013).
- ³³F. Valentini, A. Iazzolino, and P. Veltri, *Phys. Plasmas* **17**, 052104 (2010).
- ³⁴G. Birkhoff and S. Mac Lane, *A Survey of Modern Algebra*, 4th ed. (Macmillan Publishing Co., Inc, New York, NY, 1977), pp. 118–120.
- ³⁵C. Z. Cheng and G. Knorr, *J. Comput. Phys.* **22**, 330–351 (1976).
- ³⁶A. P. Matthews, *J. Comput. Phys.* **112**, 102–116 (1994).
- ³⁷R. Peyret and T. D. Taylor, *Computational Methods for Fluid Flow* (Springer, New York, 1983).
- ³⁸N. A. Krall and A. W. Trivelpiece, *Principles of Plasma Physics* (San Francisco Press, San Francisco, CA, 1986).
- ³⁹L. D. Landau, *J. Phys. U.S.S.R.* **10**, 25 (1946).
- ⁴⁰T. H. Stix, *Waves in Plasmas* (American Institute of Physics, New York, 1992).
- ⁴¹T. O'Neil, *Phys. Fluids* **8**, 2255 (1965).
- ⁴²G. Manfredi, *Phys. Rev. Lett.* **79**, 2815 (1997).
- ⁴³M. Brunetti, F. Califano, and F. Pegoraro, *Phys. Rev. E* **62**, 4109 (2000).
- ⁴⁴F. Valentini, V. Carbone, P. Veltri, and A. Mangeney, *Phys. Rev. E* **71**, 017402 (2005).
- ⁴⁵L. Rudakov, M. Mithaiwala, G. Ganguli, and C. Crabtree, *Phys. Plasmas* **18**, 012307 (2011).
- ⁴⁶L. Rudakov, C. Crabtree, G. Ganguli, and M. Mithaiwala, *Phys. Plasmas* **19**, 042704 (2012).
- ⁴⁷L. D. Landau, “The transport equation in the case of the coulomb interaction,” *Collected papers of L. D. Landau* (Pergamon Press, 1965), pp. 163–170.
- ⁴⁸O. Pezzi, F. Valentini, D. Perrone, and P. Veltri, *Phys. Plasmas* **20**, 092111 (2013).
- ⁴⁹O. Pezzi, F. Valentini, and P. Veltri, “Collisional relaxation: Landau versus Dougherty operator,” *J. Plasma Phys.* (published online).